Emulating ocean dynamic sea level by two-layer pattern scaling

Jiacan Yuan[1,2,3*], Robert E. Kopp[2,3]

1. Department of Atmospheric and Oceanic Sciences & Institute of Atmospheric Sciences, Fudan University, Shanghai, China
2. Department of Earth and Planetary Sciences, Rutgers University, New Brunswick, United States
3. Rutgers Institute of Earth, Ocean, and Atmospheric Sciences, Rutgers University, New Brunswick, New Jersey, United States

Keywords: Sea level rise, pattern scaling, thermal expansion, ocean dynamic sea level

Corresponding author: Jiacan Yuan (jcyuan@fudan.edu.cn)

Abstract

Ocean dynamic sea level (DSL) change is a key driver of relative sea level (RSL) change. Projections of DSL change are generally obtained from simulations using atmosphere-ocean general circulation models (GCMs). Here, we develop a two-layer climate emulator to interpolate between emission scenarios simulated with GCMs and extend projections beyond the time horizon of available simulations. This emulator captures the evolution of DSL changes in corresponding GCMs, especially over middle and low latitudes. Compared with an emulator using univariate pattern scaling, the two-layer emulator more accurately reflects GCM behavior and captures non-linearities and non-stationarity in the relationship between DSL and global-mean warming. Using the emulator, we develop a probabilistic ensemble of DSL projections through 2300 for four scenarios: Representative Concentration Pathway (RCP) 2.6, RCP4.5, RCP8.5, and Shared Socioeconomic Pathway (SSP) 3-7.0. The magnitude and uncertainty of projected DSL changes decrease from the high- to the low- emission scenarios, indicating a reduced DSL rise hazard in low- and moderate- emission scenarios (RCP2.6 and RCP4.5) compared to the high-emission scenarios (SSP3-7.0 and RCP8.5).

1. Introduction

Sea-level rise broadly impacts coastal communities and ecosystems through permanent inundation, increased frequency of tidal flooding, and increased frequency and severity of flooding associated with storm surge. Global-mean sea level is rising at an accelerating rate, and under most scenarios is projected to continue accelerating over the 21st century (Oppenheimer et al., 2019). Regional relative sea level (RSL) change differs from global-mean sea-level change due to a variety of processes operating on diverse timescales, including gravitational, rotational, and deformational effects associated with mass redistribution, and ocean dynamic effects associated with changes in winds, currents, and sea water density, as well as inhomogeneous changes in ocean density (Stammer et al., 2013; Perrette et al., 2013; Kopp et al., 2015; Gregory et al., 2019).

Atmosphere-ocean general circulation models (GCMs) are the primary tool used to project changes in ocean dynamic sea level (DSL)[1], but the computational demands of these models limit the utility of ensembles of GCM output for estimating the likelihood of different levels of future sea-level change. Ensembles such as the Coupled Model Intercomparison Project Phase 5 (CMIP5, Landerer et al., 2014; Taylor et al., 2012) are composed of models contributed based on voluntary effort, not the product of systematic experimental design; as such, they are an "ensemble of opportunity" rather than a probabilistic ensemble (Tebaldi and Knutti, 2007). The CMIP future projection experiments are driven by a small number of forcing scenarios – Representative Concentration Pathways (RCPs) in the case of CMIP5 – and model simulations are of different lengths; some simulations run the RCPs to the year 2100, while others extend these to 2300.

The computationally intensive nature of GCMs makes it challenging to produce large perturbed-physics ensembles that represent uncertainties in key feedback parameters, as well as to simulate forcing conditions intermediate between the RCPs. Simple climate models (SCMs) provide an alternative tool for estimating the uncertainties of future projections at the global scale, as they can capture the overall physics of climate evolution and can be run very fast even on a personal computer (Held et al., 2010; Meinshausen et al., 2011; Millar et al., 2017; Perrette

[1] Here, we follow Gregory et al. (2019), defining DSL as the height of the sea surface above the geoid. For GCM output, this is equal to the local deviation of *zos* from its global mean (which, as formally defined, should equal zero but does not equal zero in all model output).

et al., 2013). However, SCMs represent the climate at a highly aggregated (e.g., global or hemispheric) scale, and thus cannot produce spatial patterns of climate change at each time step.

Pattern scaling approaches are often used to translate the global mean surface air temperature (GSAT) change into regional-scale changes for impact analysis (Mitchell, 2003; Rasmussen et al., 2016; Santer, 1990; Tebaldi et al., 2011; Tebaldi and Arblaster, 2014). Generally speaking, pattern scaling uses a simple statistical model (often, linear regression) to relate local climatic changes to a variable such as GSAT change, assuming the patterns of local response to external forcing remain constant under increased forcing (Tebaldi and Arblaster, 2014).

Some previous studies use the pattern scaling approach to estimate the uncertainty in DSL projections (Bilbao et al., 2015; Palmer et al., 2020; Perrette et al., 2013). For example, Perrette et al. (2013) regressed DSL change on GSAT. At New York City, they found that r^2 values across models vary between 0.02 and 0.85, and also that the linear relationship between DSL and GSAT becomes weaker after the 21st century. Bilbao et al. (2015) examined the relationship between DSL and several variables, including GSAT, global-mean sea-surface temperature, ocean volume mean temperature, and global-mean thermosteric sea-level rise (GMTSLR). They found that GSAT performed best in predicting 21st-century DSL change in a high emissions scenario (RCP 8.5), while ocean-volume mean temperature and GMTSLR performed better in lower emissions scenarios (RCP 2.6 and 4.5). They speculated that this difference reflects a more important role for surface warming relative to deep warming in a more strongly forced scenario. They found that, across models and scenarios, area-weighted average root mean square error in pattern-scaled 2081-2100 DSL change ranged from ~1-3 cm.

Building upon Bilbao et al. (2015)'s speculation about the relative importance of shallow and deep warming under different scenarios, we developed a bivariate pattern scaling, which uses a multiple linear regression with two predictors: GSAT and global-mean deep ocean temperature change. The two temperature changes can be generated by a two-layer energy-balance model (TLM) (Held et al., 2010; Winton et al., 2010), which has proved to be a useful tool for understanding the responses of climate system to climate forcing (Geoffroy et al., 2013b, 2013a). Shallow and deep temperatures from a TLM have previously been employed in an emulator to extend 21st century CMIP5 projections of GMTSLR to 2300 (Palmer et al., 2018),

and Palmer et al. (2020) used GSAT from the two-layer model and univariate pattern scaling to emulate CMIP5 projections of DSL change.

In this study, we develop an emulator for DSL changes using both GSAT and deep-ocean temperature change projected by a TLM. Whereas Palmer et al. (2018, 2020) exogenously specified radiative forcing, here we drive the TLM with radiative forcings from the Finite Amplitude Impulse Response model (FaIR), a simple climate model which includes a reduced-complexity carbon cycle and calculates atmospheric CO_2 concentrations, radiative forcing and temperature changes based on emissions (Millar et al., 2017; Smith et al., 2018, 2017). FaIR was adopted to more accurately reflect the temporal evolution of GSAT in response to a pulse emission, and it has been used in previous studies to produce observation-constrained future projections for estimating the uncertainties in equilibrium climate sensitivity and transient climate responses (Millar et al., 2017; Smith et al., 2018, 2017). In this study, we develop an emulator for GMTSLR and DSL projections using surface and deep-ocean temperature changes generated by the FaIR-two layer model (FaIR-TLM, section 2.2). We employ FaIR-TLM and two-layer pattern scaling to project future DSL changes, taking into account uncertainty in climate sensitivity, and demonstrates its ability to interpolate between climate scenarios run by GCMs.

Section 2 describes data and methodology, including the details of FaIR-TLM, calibration of the FaIR-TLM based on selected CMIP5 GCMs, the two-layer pattern scaling, and the approach of emulating the DSL projections. Section 3 evaluates the performance of the two-layer pattern scaling. Section 4 shows the resulting ensemble of DSL projections. Finally, section 5 discusses and summarizes the results.

2. Data and methods

2.1 Data

We use the *zos* variable from five CMIP5 general circulation models (GCMs) in RCP 2.6, 4.5, and 8.5 scenarios: MPI-ESM-LR, bcc-csm1-1, HadGEM2-ES, GISS-E2-R, IPSL-CM5A-LR. These five GCMs are used because they were used to calibrate the parameters of the TLM by Geoffroy et al. (2013) and also provide multi-century data (to 2300) for *zos* in all three scenarios. DSL is taken as zos with its global mean removed, consistent with the definition of Gregory et al. (2019). Therefore, DSL does not include global mean changes; we focus on emulating ocean

dynamic deviations from the GMTSLR. In addition, we remove the climatology in a baseline period (1986-2005) from DSL. The global mean surface air temperature (GSAT) and GMTSLR from the five models in the three scenarios are also used to evaluate the performance of FaIR-TLM.

2.2 FaIR-two layer model (FaIR-TLM) and calibration

This study develops a hybrid SCM model by replacing the temperature module in FaIR model with a TLM that includes an efficacy term for deep ocean heat uptake (Geoffroy et al., 2013a; Held et al., 2010; Winton et al., 2010):

$$C\frac{dT}{dt} = \mathcal{F} - \lambda T - \epsilon\gamma(T - T_0) \quad (1)$$

$$C_0\frac{dT_0}{dt} = \gamma(T - T_0) \quad (2)$$

where $\mathcal{F}$ denotes the adjusted radiative forcing, C and C_0 are the heat capacity of the well-mixed upper layer and the deep ocean layer, respectively, and T and T_0 represent the global mean temperature anomalies of the upper and lower layer, respectively. T is equivalent to GSAT perturbation (Held et al., 2010). λ is the parameter for climate feedback, γ is the coefficient of deep ocean heat uptake, and ε is the efficacy factor of deep ocean heat uptake, which represents the uneven spatial distribution of heat exchanges between the two layers.

The FaIR model used in this study is version 1.3, described by Smith et al. (2018). In FaIR 1.3, the changes of GSAT are the sum of two components, representing fast and slow responses to effective radiative forcing (ERF) (equation 22 in Smith et al., 2018). The fast and slow components of temperature changes in FaIR 1.3 mathematically depend on multiple coefficients (e.g., thermal response timescales) that are obtained from the ensemble mean of multiple CMIP5 models (Geoffroy et al., 2013b). The fast and slow components do not have an unambiguous physical meaning, so it is challenging to link them to sea-level change. Therefore, we replace the temperature module in FaIR 1.3 by the TLM to construct FaIR-TLM. In each step of FaIR-TLM, the TLM is driven by radiative forcing from FaIR 1.3, and produces the GSAT anomaly, which feeds back to the FaIR carbon cycle (Figure S1).

To calibrate FaIR-TLM, we adjust parameter settings (listed in Table 1) based on previous studies (Forster et al., 2013; Geoffroy et al., 2013a; Zelinka et al., 2014). The radiative forcing in FaIR-TLM is driven by the default emission trajectory for each scenario in FaIR 1.3, but scaled

by two parameters determined for each GCM: (1) the radiative forcing of CO_2 doubling ($F_{2\times CO_2}$) reported by Forster et al. (2013), and (2) the present-day aerosol forcing (af_{pd}) estimated in previous studies (Forster et al., 2013; Zelinka et al., 2014), or -0.9 W m^{-2} – the median of range estimated by the Fifth Assessment Report of Intergovernmental Panel on Climate Change (IPCC AR5) (Stocker et al., 2013) – for models not reported in previous studies. The five parameters in equation 1 and 2 (i.e. $\lambda, \gamma, \epsilon$, C, C_0) are the same as those in Geoffroy et al. (2013) for the corresponding GCMs.

GSAT produced by the calibrated FaIR-TLM is compared with that from the corresponding GCMs in the three scenarios (Fig. S2). For the five GCMs, the GSAT simulated by FaIR-TLM is close to the GSAT from the corresponding GCM, with the root mean square error (RMSE) in a range of 0.15 – 0.23 K for RCP2.6, 0.14-0.32 K for RCP4.5, and 0.2 -0.43 K for RCP8.5.

GMTSLR is driven by the thermal expansion of sea water volume due to the increase in ocean heat uptake. To calibrate GMTSLR in FaIR-TLM to match a specific GCM, we first correct the drift in the GCM's GMTSLR field by removing the linear trend in the pre-industrial control simulation, assuming the drift is not sensitive to the external forcing (Hobbs et al., 2016). Then, we emulate GMTSLR based on the T and T_0 from FaIR-TLM following the approach described in Kuhlbrodt and Gregory (2012):

$$GMTSLR = \sigma * (C\Delta T + C_0\Delta T_0) \quad (3)$$

where σ is the expansion efficiency of heat in units of 10^{-24} m J^{-1}. The σ value is calibrated by optimizing GMTSLR emulated from FaIR-TLM to match the GMTSLR simulated from the corresponding GCM.

2.3 Two-layer pattern scaling

Univariate pattern scaling is based on a linear relation between the changes in a climate variable (DSL for this study) and the changes in a single variable, such as GSAT (T):

$$DSL(t,x,y) = \alpha(x,y)T(t) + b(x,y) + \varepsilon(t,x,y) \quad (4)$$

where x and y denote longitudes and latitudes, t represents time, b is an intercept term, and ε is the residual term. Here, α captures the scaling relationship between DSL and GSAT (Fig. 1). The five GCMs agree that the linear response of DSL to warming is positive over the Arctic and sub-

polar Atlantic, and negative over the southeastern Pacific and the southern areas of Southern Ocean.

In the bivariate pattern scaling approach, we regress the DSL anomaly on both ΔT (GSAT anomaly) and T_0 (deep-ocean temperature anomaly) from FaIR-TLM:

$$DSL(t_i, x, y) = \alpha(x, y)T(t_i) + \beta(x, y)T_0(t_i) + b(x, y) + \varepsilon(t_i, x, y) \quad (5)$$

where t_i denotes years in three scenarios, *i*=1, 2, 3. For each GCM, we estimate the fields of α, β, b and ε by regressing projections from all three emissions scenarios (RCPs 2.6, 4.5, and 8.5) on T and T_0 on a grid cell-by-grid cell basis. α represents changes in *zos* in response to changes in surface temperature in the period 1981-2300, while β represents the response of changes in *zos* to changes in deep-ocean temperature at the same period (Fig. 1). The five GCMs agree that the fast response represented by α is positively correlated with warming over the most areas of Arctic and northern edge of the Southern Ocean, and negatively correlated with warming over the southeastern Pacific and the southern areas of Southern Ocean, while the slow response represented by β is positively correlated with warming over the Indian and tropical and southern Pacific Oceans, and negatively correlated with warming over most areas of the Southern Ocean and Arctic. These reflect opposite behaviors between rapid and sustained changes in DSL over the Arctic, the Indian and tropical and southern Pacific Oceans, and a consistent DSL fall in both rapid and sustained changes over the Southern Ocean.

2.4 Projecting DSL using FaIR-TLM and patterns

We use two steps to generate a probabilistic ensemble of DSL projections. First, we generate an ensemble of surface and deep-ocean temperature pairs using FaIR-TLM as follows. The planetary energy balance at the top of the atmosphere (Zelinka et al., 2020) is:

$$N = \mathcal{F} + \lambda T \quad (6)$$

Where *N* is the radiative imbalance at the top of the atmosphere. The equilibrium climate sensitivity (ECS) is given by *T* when *N* = 0, and $\mathcal{F}$ = F_{2XCO2}. Therefore, λ is related to F_{2XCO2} and ECS by

$$\lambda = -F_{2XCO2}/ECS \quad (7)$$

The uncertainty of $F_{2\times CO_2}$ is small relative to the spread of λ, while ECS largely determine the uncertainty of λ. Therefore, we adopt the best estimation in the Intergovernmental Panel on

Climate Change Fifth Assessment Report (AR5) for $F_{2\times CO_2}$ = 3.71 $W\ m^{-2}$ (Collins et al., 2013). We produce initial distributions of ECS, γ, and $\gamma\epsilon$ based on the literature constraints (Fig. S4) outlined below:

ECS: Based on multiple lines of evidence, the uncertainties of ECS estimated by AR5 are *likely* in the range 1.5°C to 4.5°C with high confidence, extremely unlikely less than 1°C and very unlikely greater than 6°C (Collins et al., 2013). In the AR5 terminology, *likely* denotes a probability of at least 66%, *very unlikely* a probability of less than 10%, and *extremely unlikely* a probability of less than 5% (Mastrandrea et al., 2010). Therefore, we construct a log-normal distribution for ECS with parameterized optimized to match a 5th percentile of 1°C, a 17th percentile of 1.5°C, an 83rd percentile of 4.5°C, and a 90th percentile of 6°C.

γ: We construct the distribution of γ as a normal distribution with mean 0.67 $W\ m^{-2}\ K^{-1}$ and standard deviation 0.15 $W\ m^{-2}\ K^{-1}$, based on the 16 GCMs from CMIP5 archive (Geoffroy et al. 2013).

$\gamma\varepsilon$: We calculate the mean and standard deviation of $\gamma\varepsilon$ based on the products of γ and ε from the GCMs (Geoffroy et al., 2013a). We do not consider their covariance. The distribution of $\gamma\varepsilon$ is constructed as a normal distribution with a mean of 0.86 $W\ m^{-2}\ K^{-1}$ and a standard deviation of 0.29 $W\ m^{-2}\ K^{-1}$.

Based on the multi-model mean of GCMs from Coupled Model Intercomparison Project Phase 5 (CMIP5) archive, we set C = 8.2 $W\ yr\ m^{-2}\ K^{-1}$ and C_0 = 109 $W\ yr\ m^{-2}\ K^{-1}$ (Geoffroy et al., 2013a). While there are significant uncertainties of these parameters among GCMs, fixed values are used because the uncertainties of these parameters are not necessary to represent uncertainty in the Transient Climate Response (TCR), which can be constrained adequately by varying only λ and $\gamma\varepsilon$ under the zero-layer approximation which considers the 1%/yr increase in CO_2 until doubling scenario occurring on a timescale long enough that the upper ocean is in approximate equilibrium and short enough that the deep-ocean temperature has not yet responded substantially (Jiménez-de-la-Cuesta and Mauritsen, 2019):

$$TCR = -\frac{F_{2\times CO2}}{\lambda - \gamma\varepsilon} \tag{8}$$

We then generate a 100,000-member ensemble of parameter sets based on these distributions via Monte Carlo sampling. As $\gamma\varepsilon$ should be larger than 0, we discard parameter sets in which $\gamma\epsilon < 0$ or $\gamma\epsilon > 2 \times 0.86$ to keep the mean of $\gamma\epsilon$ in parameter sets to be 0.86

$W\ m^{-2}\ K^{-1}$. Therefore, 99734 parameter sets are kept. An ensemble of λ is then computed by the best estimation of F_{2XCO2} and the ensemble of ECS based on equation 6 (Fig. S4). The median (*central* 66% range) of λ is -1.39 (-2.4 – -0.8) $W\ m^{-2}\ K^{-1}$. As the *likely* range of ECS estimated by AR5 is equivalent to the central 90% range of ECS estimated by CMIP5 GCMs, the uncertainty range of λ estimated by FaIR-TLM is larger than that estimated by ensemble of GCMs（Geoffroy et al. 2013). The spread of TCR is estimated by substituting then ensemble of λ, $\gamma\varepsilon$, and best estimation of F_{2XCO2} into equation 7. The uncertainty of TCR is in a central 66% range of 1.1– 2.3 ℃, with a 95th percentile of 2.9℃. Comparing with the TCR estimated by AR5 which is *likely* between 1 ℃ and 2.5 ℃, and is *extremely unlikely* greater than 3℃, the range of TCR emulated by FaIR-TLM is slightly narrower.

We apply Latin hypercube sampling (LHS, Stein, 1987) approach to the parameter sets of λ, γ, $\gamma\epsilon$ by sampling 1000 sets from the 99734 parameter sets. For each parameter, LHS divides the probability density function of the 99734 samples into 1000 portions that have equal area. A sample is taken from each portion randomly so that the 1000 sample sets cover the multidimensional distribution of the three parameters. Finally, we applied 1000 parameter sets together with the fixed parameters (F_{2XCO2}, C, C_0) to the FAIR-TLM and generate a 1000-member ensemble of temperature pair time-series.

We compare the spread in GSAT projected by FaIR-TLM with the *likely* ranges assessed by estimated by AR5 for four different periods (Collins et al., 2013) (Table 2 and Fig. S5) . The mean of 1000-member ensemble is slightly lower than the mean estimate of GSAT from AR5 in all four periods of RCP2.6 and RCP4.5, and in the 21st century for RCP8.5. Compared with AR5 likely ranges, the central 66% probability range of GSAT from FaIR-TLM is generally consistent: narrower in all four periods of RCP2.6, narrower in the first two periods but wider in the last two periods in RCP4.5, and wider in the first two periods but narrower in the last two periods in RCP8.5.

We project GMTSLR based on the equation 3 using the 1000-member ensemble of surface and deep-ocean temperature projections from FaIR-TLM. The C, C_0 and expansion efficiency of heat σ used here are 8.2 $W\ yr\ m^{-2}\ K^{-1}$, 109 $W\ yr\ m^{-2}\ K^{-1}$, and 0.113×10^{-24} m J^{-1} adopted from the multi-model ensemble mean of CMIP5 archive (Geoffroy et al., 2013a; Kuhlbrodt and Gregory, 2012) .

A projection of DSL is constructed as follows: 1) a pair of α and β is randomly picked with replacement from the pool of two-layer patterns produced in section 2.3; 2) a temperature pair from the 1000 members is combined with the pair of α and β in an equation

$$DSL(t,x,y) = \alpha(x,y)T(t) + \beta(x,y)T_0(t) + b(x,y) \quad (5)$$

where the regression coefficients have been previously estimated as in equation (5).

3. Evaluation of two-layer pattern scaling

To evaluate the prediction skill of the two-layer pattern scaling, we compare DSL predicted by two-layer pattern scaling ($\widehat{DSL}$) with the DSL simulated from the corresponding GCM using two metrics: (1) absolute values of the residual differences between climatology of $\widehat{DSL}$ and climatology of *DSL* during a period at each grid point, and (2) global average of the absolute values obtained from the metric 1 (Table S1). These two metrics are applied to both bivariate pattern scaling and univariate pattern scaling on *T*.

In 2271-2290, for instance, $R = DSL - \widehat{DSL}$ for an individual GCM are smaller than DSL in magnitude in both univariate and two-layer pattern scaling approaches (Fig. S6-S10). The 5-model ensemble averaged climatology of $|R|$ in both approaches is higher over high latitudes (e.g. Arctic, subpolar Northern Atlantic, Southern Ocean) than over middle to low latitudes, but is generally lower in two-layer pattern scaling than in univariate pattern scaling (first two rows Fig. 2). The global-averaged $\left|DSL - \widehat{DSL}\right|$ (*Score* obtained by the second metric) from the two-layer pattern scaling is less than that from the univariate pattern scaling (bottom row Fig. 2), indicating reduced errors of predicted by two-layer approach in all three scenarios.

We further compared the time evolving of DSL predicted by the two-layer pattern scaling approaches with the evolving DSL in corresponding GCMs through the period 1981-2290. As case studies, we pick two grid cells: one in the western Pacific near the Philippines (14.5°N, 127°E), and the other over the North Atlantic near the coast of New York City [NYC] (40°N, 73°W) (solid black dots in Fig. 2). At the grid cell over western Pacific, in RCP 2.6, responses of DSL to GSAT anomaly display a hook-like shape, indicating continued rise in DSL as GSAT stabilizes and declines in response to negative emissions (Fig. 3a). Across the five GCMs, responses of DSL to increases in GSAT are diverse in RCP4.5 and RCP8.5. At the North Atlantic grid cell, the responses of DSL to GSAT also display non-linear features for all the five

models, especially in low- and moderate- emission scenarios (Fig. 3b). These highly non-linear features of DSL in response to GSAT anomaly cannot be captured by univariate pattern scaling but are captured to a large extent by the two-layer pattern scaling (lines in Fig. 3). The value of the two-layer approach is highlighted by the clear non-linearity of the DSL response when viewed as a function of GSAT anomaly. The two-layer pattern scaling includes one more predictor than univariate pattern scaling, allowing it to capture the delayed adjustment of DSL. Therefore, the method of two-layer pattern scaling generally has a better performance on emulating the DSL from the corresponding GCM than the univariate pattern scaling.

4. Projections of DSL

The procedure described in section 2.4 allows us to produce 1000-member ensemble of DSL projections not only for the three CMIP5 scenarios: RCP2.6, RCP4.5 and RCP8.5, but also for any other scenarios with an emission pathway between these three scenarios. We demonstrate this capability using SSP3-7.0, a CMIP6 scenario that has forcing intermediate between RCP4.5 and RCP8.5 (O'Neill et al., 2016). The emission pathway of SSP3-7.0 used to drive the FaIR-TLM is from the Reduced Complexity Model Intercomparison Project (https://www.rcmip.org).

The five projections using parameters calibrated to the five GCMs respectively are within the 66% range of the 1000-member ensemble for both surface and deep-ocean temperature in the three RCPs (Figure 4). During the period of 2081-2100, the median estimates (66% range) of the surface temperature relative the period of 1986-2005 are aligns reasonably well with the central 66%-range spread of GSAT projections estimated by IPCC AR5 for the three RCP scenarios (Table 2). By 2300, the median estimates (66% range) of the surface temperature relative the period of 1986-2005 are 0.5℃ (0.2-1.0℃) for RCP2.6, 2.2℃ (1.2-3.6℃) for RCP4.5, 7.4℃ (4.5-11.7℃) for RCP8.5, and 5.3℃ (3.2-8.6℃) for SSP3-7.0.

Based on the projections of temperature pairs, we also produced projections of GMTSLR for the 4 scenarios (Fig. 4). The spread of GMTSLR ensemble encapsulates the GMTSLR time series from the 5 GCMs (Figure 5). During the period of 2081-2100, the median estimates (66% range) of the GMTSLR relative the period of 1986-2005 are 0.12m (0.07-0.18m) for RCP2.6, 0.16m (0.10-0.24m) for RCP4.5, 0.24m (0.15-0.34m) for RCP8.5, and 0.19m (0.12-0.27m) for SSP3-7.0. This compares to AR5 projected median estimates (66% ranges) of 0.14m (0.10-0.18m) for RCP2.6, 0.19m(0.14-0.23m) for RCP4.5, 0.27m (0.21-0.33m) for RCP8.5

(Oppenheimer et al. 2019). By 2300, the median estimates (66% range) of GMTSLR relative to the period of 1986-2005 are 0.20m (0.12-0.33m) for RCP2.6, 0.43m (0.25-0.68m) for RCP4.5, 1.15m (0.69-1.76m) for RCP8.5, 0.85m (0.50-1.33m) for SSP3-7.0. Compared with the GSAT and GMTSLR spread in 2300 estimated by Palmer et al. (2018), the FaIR-TLM projections have a slightly lower median for all the three RCPs. The 66% range of both surface temperature and GMTSLR estimated by FaIR-TLM is comparable to the 90% range of that estimated by Palmer et al. (2018) because we adopt a distribution of λ based on the AR5 assessment of equilibrium climate sensitivity (Collins et al., 2012), which relaxes the 90% range estimated by the CMIP5 multi-model ensemble emulated by Palmer et al. (2018).

Comparing the DSL projections between the period of 2081-2100 and the period of 2271-2290 (Fig. 5), the median estimation is lower and the 66% range of uncertainty is narrower by the end of 21st century than that by the end of 23rd century in moderate- to high- emission scenarios (RCP4.5, SSP3-7.0 and RCP8.5). But in RCP2.6, the median estimation and 66% uncertainty range are comparable in magnitude between these two periods. In both periods, the median DSL anomaly projections across the four scenarios share many similar features (Fig. 5). Over the Arctic region, a weak increase in DSL is observed over the Chukchi Sea and the Beaufort Sea in RCP2.6. In the higher emission scenarios, the increase in DSL extends to the whole Arctic basin with intensified amplitudes. The changes in DSL over the North Atlantic are dominated by a negative anomaly under RCP2.6, and display positive anomalies over much of the North Atlantic under RCP8.5 and SSP3-7.0. The ensemble spread of the 5th-95th range of DSL projections are relatively large over the Southern Ocean, Arctic and Subpolar Atlantic than other areas. The large uncertainties over these areas, consistent with previous literatures (Palmer et al., 2020; Perrette et al., 2013; Yin, 2012), may be interpreted by the diverse characteristics simulated by GCMs due to the challenges of capturing complex physical process over these areas.

Again, we take two grid points as examples to display the ensemble projection of DSL changes relative to the baseline period 1986-2005 (Fig. 6). At the grid point near Philippines over western Pacific, the 66% range of the 1000-member ensemble can only encapsulate DSL projections from 2 over 5 GCMs in the three RCPs. They are GISS-E2-R and bcc-csm1-1. The 90% range of the 1000-member ensemble can encapsulate DSL projections from all the 5 GCMs in the three RCPs, except for HadGEM2-ES in RCP2.6. At the grid point near NYC over the North Atlantic, the projected DSL changes estimated by the 1000-member ensemble represent a

high risk of DSL rise in high-emission scenarios (i.e. RCP8.5 and SSP3-7.0). The low-emission scenario (i.e. RCP2.6) could largely decrease the risk of DSL rise with a slight DSL decline in 2300 by the median estimation. The 66% range of the projected DSL uncertainties fails to encapsulating most of the DSL projections by the 5 GCMs in RCP2.6 and RCP4.5, and only fully encapsulates 2 of 5 projected DSL by GCMs. The 90% range of the 1000-member ensemble only encapsulates the DSL projections from three over five GCMs in RCP2.6 and RCP4.5, but encapsulates the DSL projections from all five GCMs in RCP8.5. The emulator fails to capture multidecadal variability in DSL, a limitation which would be expected based on the simple construction of the emulator.

5. Discussion and conclusions

We have developed a probabilistic ensemble of DSL projections through 2300 using a novel two-layer emulator. Replacing the climate module in the FaIR simple climate model with a two-layer energy-balance model, we developed FaIR-TLM, which produces projections of global average temperature in the well-mixed upper layer (T) for fast responses to radiative forcing, and in the deep ocean layer (T_0) for slow responses. Calibrated by the parameters for each GCMs, the GSAT (Fig. S2) and global mean thermosteric sea level change (Fig. S3) emulated by FaIR-TLM generally follow that from the corresponding GCM, with RMSE<0.43 K for GSAT and RMSE<0.05 m for GMTSLR. A two-layer pattern scaling based on surface and deep-ocean temperature is used to project DSL. During the period 2271-2290, for instance, the DSL predicted by the two-layer pattern scaling are more close to the DSL simulated by the corresponding GCM than that predicted by the univariate pattern scaling, because the two-layer pattern scaling can capture the non-linear responses of DSL to climate warming (Fig. 2, 3).

By perturbating the key parameters, FaIR-TLM allows emulation of projected global-mean surface and deep-ocean temperature pairs and GMTSLR for emissions scenarios (e.g., SSP3-7.0; Fig. 4 and 5) beyond those run by the GCMs to which it is calibrated. Compared with the likely ranges assessed by AR5 in the RCP 2.6, 4.5 and 8.5, the FaIR-TLM performs well in emulating the GSAT spread (Table 2 and Fig. S5). By 2300, the ensembles of GSAT and GMTSLR estimated by FaIR-TLM have a slightly lower median and a slightly wider 90% range than the estimations by Palmer et al. (2018). These differences might be due to 1) we use the uncertainty of ECS from AR5 which has a larger range than that estimated by CMIP5 multi-model ensemble,

to derive the distribution of λ; 2) more complex processes are considered by the FaIR-TLM than the TLM used in Palmer et al. (2018), such as the efficacy factor of deep ocean heat uptake and coupled carbon cycle.

We produce 1000-member ensembles of DSL projections for four different emissions scenarios. Characteristics of median DSL projections during 2271-2290 include increases in DSL along most of the coast around the Pacific and Indian Oceans and a decrease in DSL over the Southern Ocean in all four scenarios, as well as increased DSL over the Arctic and along the North Atlantic Current in moderate to high emissions scenarios (Fig. 5). The 90% range (5^{th}-95^{th} percentile) of uncertainties are small over the middle and low latitudes, and are relatively large over the Southern Ocean, Arctic and North Atlantic, where the simulations of GCMs are diverse due to the challenges of capturing the complex physical processes, such as deep water formation in the subpolar Atlantic, the Antarctic circumpolar current, and ice-albedo feedback in polar regions (Flato et al., 2013; Landerer et al., 2014; Wang et al., 2014). The ensemble of DSL projections also allows us to examine the trajectories of the DSL projections and their uncertainties at specific locations (Fig. 6). At selected locations in the North Atlantic and Western Pacific, the 90% range of DSL spread generally encapsulates the time series of DSL changes relative to the baseline period from the 5 GCMs.

The two-layer emulator provides a useful tool to explore the uncertainty of DSL projections over multiple centuries with computational resources that are much less than a GCM requires. It can be calibrated to match assessments of key values like the equilibrium climate sensitivity, and allows the flexibility of simulating forcing conditions intermediate between the RCPs as the patterns are common for different scenarios. However, we should note that the errors between the DSL predicted by two-layer emulator and DSL simulated by the corresponding GCMs are small in middle and low latitudes but relatively large in high latitudes (e.g. the Southern Ocean, Arctic, and subpolar Atlantic). Thus, DSL emulated by the two-time scale approach in high latitudes with caution.

Acknowledgement

Jiacan Yuan and Robert E. Kopp were supported by a grant from the Rhodium Group (for whom REK has previously worked as a consultant) as part of the Climate Impact Lab consortium.

Jiacan Yuan was also supported by Shanghai Municipal Natural Science Fund (20ZR1407400). Robert E. Kopp was also supported by grants from the National Science Foundation (ICER-1663807) and the National Aeronautics and Space Administration (80NSSC17K0698). We acknowledge the World Climate Research Programmer's Working Group on Coupled Modeling, which is responsible for CMIP, and we thank the climate modeling groups (listed in section 2.2) for producing and making available their model output. For CMIP, the U.S. Department of Energy's Program for Climate Model Diagnosis and Intercomparison provides coordinating support and leads development of software infrastructure in partnership with the Global Organization for Earth System Science Portals. We would like to thank the developers of FaIR for the open-source code which allows us to incorporate FaIR in the emulator.

Data availability statement

The result data that support the findings of this study are available on Figshare repository (https://doi.org/10.6084/m9.figshare.12885584). The python scripts used in this work are posted on Github: https://github.com/Jiacan/FAIR-TLM-emulator.

Reference

Bilbao, R.A.F., Gregory, J.M., Bouttes, N., 2015. Analysis of the regional pattern of sea level change due to ocean dynamics and density change for 1993–2099 in observations and CMIP5 AOGCMs. Clim. Dyn. 45, 2647–2666. https://doi.org/10.1007/s00382-015-2499-z

Collins, M., Knutti, R., Arblaster, J., Dufresne, J.-L., Fichefet, T., Friedlingstein, P., Gao, X., Gutowski, W.J., Johns, T., Krinner, G., Shongwe, M., Tebaldi, C., Weaver, A.J., Wehner, M., 2013. Long-term climate change: Projections, commitments and irreversibility, in: IPCC (Ed.), Climate Change 2013: The Physical Science Basis. IPCC Working Group I Contribution to AR5. Cambridge University Press, Cambridge.

Drijfhout, S., Bathiany, S., Beaulieu, C., Brovkin, V., Claussen, M., Huntingford, C., Scheffer, M., Sgubin, G., Swingedouw, D., 2015. Catalogue of abrupt shifts in Intergovernmental Panel on Climate Change climate models. Proc. Natl. Acad. Sci. 112, E5777–E5786. https://doi.org/10.1073/pnas.1511451112

Flato, G., Marotzke, J., Abiodun, B., Braconnot, P., Chou, S.C., Collins, W., Cox, P., Driouech, F., Emori, S., Eyring, V., Forest, C., Gleckler, P., Guilyardi, E., Jakob, C., Kattsov, V., Reason, C., Rummukainen, M., 2013. Evaluation of Climate Models, in: Climate Change 2013: The Physical Science Basis. Contribution of Working Group I to the Fifth Assessment Report of the Intergovernmental Panel on Climate Change. Cambridge University Press, Cambridge, United Kingdom and New York, NY, USA.

Forster, P.M., Andrews, T., Good, P., Gregory, J.M., Jackson, L.S., Zelinka, M., 2013. Evaluating adjusted forcing and model spread for historical and future scenarios in the CMIP5 generation of climate models. J. Geophys. Res. Atmospheres 118, 1139–1150. https://doi.org/10.1002/jgrd.50174

Geoffroy, O., Saint-Martin, D., Bellon, G., Voldoire, A., Olivié, D.J.L., Tytéca, S., 2013a. Transient Climate Response in a Two-Layer Energy-Balance Model. Part II: Representation of the Efficacy of Deep-Ocean Heat Uptake and Validation for CMIP5 AOGCMs. J. Clim. 26, 1859–1876. https://doi.org/10.1175/JCLI-D-12-00196.1

Geoffroy, O., Saint-Martin, D., Olivié, D.J.L., Voldoire, A., Bellon, G., Tytéca, S., 2013b. Transient Climate Response in a Two-Layer Energy-Balance Model. Part I: Analytical Solution and Parameter Calibration Using CMIP5 AOGCM Experiments. J. Clim. 26, 1841–1857. https://doi.org/10.1175/JCLI-D-12-00195.1

Held, I.M., Winton, M., Takahashi, K., Delworth, T., Zeng, F., Vallis, G.K., 2010. Probing the Fast and Slow Components of Global Warming by Returning Abruptly to Preindustrial Forcing. J. Clim. 23, 2418–2427. https://doi.org/10.1175/2009JCLI3466.1

Hobbs, W., Palmer, M.D., Monselesan, D., 2016. An Energy Conservation Analysis of Ocean Drift in the CMIP5 Global Coupled Models. J. Clim. 29, 1639–1653. https://doi.org/10.1175/JCLI-D-15-0477.1

Jiménez-de-la-Cuesta, D., Mauritsen, T., 2019. Emergent constraints on Earth's transient and equilibrium response to doubled CO 2 from post-1970s global warming. Nat. Geosci. 12, 902–905. https://doi.org/10.1038/s41561-019-0463-y

Kuhlbrodt, T., Gregory, J.M., 2012. Ocean heat uptake and its consequences for the magnitude of sea level rise and climate change. Geophys. Res. Lett. 39. https://doi.org/10.1029/2012GL052952

Landerer, F.W., Gleckler, P.J., Lee, T., 2014. Evaluation of CMIP5 dynamic sea surface height multi-model simulations against satellite observations. Clim. Dyn. 43, 1271–1283. https://doi.org/10.1007/s00382-013-1939-x

Meinshausen, M., Raper, S.C.B., Wigley, T.M.L., 2011. Emulating coupled atmosphere-ocean and carbon cycle models with a simpler model, MAGICC6 – Part 1: Model description and calibration. Atmos Chem Phys 11, 1417–1456. https://doi.org/10.5194/acp-11-1417-2011

Millar, R.J., Nicholls, Z.R., Friedlingstein, P., Allen, M.R., 2017. A modified impulse-response representation of the global near-surface air temperature and atmospheric concentration response to carbon dioxide emissions. Atmospheric Chem. Phys. 17, 7213–7228. https://doi.org/10.5194/acp-17-7213-2017

Mitchell, T.D., 2003. Pattern Scaling: An Examination of the Accuracy of the Technique for Describing Future Climates. Clim. Change 60, 217–242. https://doi.org/10.1023/A:1026035305597

Palmer, M.D., Gregory, J.M., Bagge, M., Calvert, D., Hagedoorn, J.M., Howard, T., Klemann, V., Lowe, J.A., Roberts, C.D., Slangen, A.B.A., Spada, G., 2020. Exploring the Drivers of Global and Local Sea-Level Change over the 21st Century and Beyond. Earths Future n/a, 2328–4277. https://doi.org/10.1029/2019EF001413

Perrette, M., Landerer, F., Riva, R., Frieler, K., Meinshausen, M., 2013. A scaling approach to project regional sea level rise and its uncertainties. Earth Syst. Dyn. 4, 11–29. https://doi.org/10.5194/esd-4-11-2013

Rasmussen, D.J., Meinshausen, M., Kopp, R.E., 2016. Probability-Weighted Ensembles of U.S. County-Level Climate Projections for Climate Risk Analysis. J Appl Meteor Clim. 55, 2301–2322. https://doi.org/10.1175/JAMC-D-15-0302.1

Santer, B.D., 1990. Developing climate scenarios from equilibrium GCM results. Max-Planck-Institut für Metrologie.

Smith, C.J., Forster, P.M., Allen, M., Leach, N., Millar, R.J., Passerello, G.A., Regayre, L.A., 2018. FAIR v1.3: a simple emissions-based impulse response and carbon cycle model. Geosci Model Dev 11, 2273–2297. https://doi.org/10.5194/gmd-11-2273-2018

Smith, C.J., Forster, P.M., Allen, M., Leach, N., Millar, R.J., Passerello, G.A., Regayre, L.A., 2017. FAIR v1.1: A simple emissions-based impulse response and carbon cycle model. Geosci Model Dev Discuss 2017, 1–45. https://doi.org/10.5194/gmd-2017-266

Stein, M., 1987. Large Sample Properties of Simulations Using Latin Hypercube Sampling. Technometrics 29, 143–151. https://doi.org/10.1080/00401706.1987.10488205

Stocker, Thomas.F., Qin, D., Plattner, G.-K., Tignor, M.M.B., Allen, S.K., Boschung, J., Nauels, A., Xia, Y., Bex, V., Midgley, P.M., 2013. Climate Change 2013: The Physical Science Basis. Contribution of Working Group I to the Fifth Assessment Report of the Intergovern- mental Panel on Climate Change. Cambridge University Press, Cambridge, UK and New York, NY, USA.

Taylor, K.E., Stouffer, R.J., Meehl, G.A., 2012. An Overview of CMIP5 and the Experiment Design. Bull. Am. Meteorol. Soc. 93, 485–498. https://doi.org/10.1175/BAMS-D-11-00094.1

Tebaldi, C., Arblaster, J.M., 2014. Pattern scaling: Its strengths and limitations, and an update on the latest model simulations. Clim. Change 122, 459–471. https://doi.org/10.1007/s10584-013-1032-9

Tebaldi, C., Arblaster, J.M., Knutti, R., 2011. Mapping model agreement on future climate projections. Geophys. Res. Lett. 38, L23701. https://doi.org/10.1029/2011GL049863

Tebaldi, C., Knutti, R., 2007. The use of the multi-model ensemble in probabilistic climate projections. Philos. Trans. R. Soc. Lond. Math. Phys. Eng. Sci. 365, 2053–2075. https://doi.org/10.1098/rsta.2007.2076

Wang, C., Zhang, L., Lee, S.-K., Wu, L., Mechoso, C.R., 2014. A global perspective on CMIP5 climate model biases. Nat. Clim. Change 4, 201–205. https://doi.org/10.1038/nclimate2118

Winton, M., Takahashi, K., Held, I.M., 2010. Importance of Ocean Heat Uptake Efficacy to Transient Climate Change. J. Clim. 23, 2333–2344. https://doi.org/10.1175/2009JCLI3139.1

Yin, J., 2012. Century to multi-century sea level rise projections from CMIP5 models. Geophys. Res. Lett. 39. https://doi.org/10.1029/2012GL052947

Zelinka, M.D., Andrews, T., Forster, P.M., Taylor, K.E., 2014. Quantifying components of aerosol-cloud-radiation interactions in climate models. J. Geophys. Res. Atmospheres 119, 7599–7615. https://doi.org/10.1002/2014JD021710

Zelinka, M.D., Myers, T.A., McCoy, D.T., Po-Chedley, S., Caldwell, P.M., Ceppi, P., Klein, S.A., Taylor, K.E., 2020. Causes of Higher Climate Sensitivity in CMIP6 Models. Geophys. Res. Lett. 47, e2019GL085782. https://doi.org/10.1029/2019GL085782

549 Table 1 FaIR-TLM parameters adjusted to match the GSAT in CMIP5 GCMs. λ ($W\ m^{-2}\ K^{-1}$),
550 γ ($W\ m^{-2}\ K^{-1}$), ϵ, C ($W\ yr\ m^{-2}\ K^{-1}$) and C_0($W\ yr\ m^{-2}\ K^{-1}$) are reported by Geoffroy et al.
551 (2013). The units for $F_{2\times CO_2}$ and af_{pd} are $W\ m^{-2}$.
552

CMIP5 GCMs	λ	γ	ϵ	C	C_0	$F_{2\times CO_2}$	af_{pd}
bcc-csm1-1	1.28	0.59	1.27	8.4	56	3.23	-0.9
GISS-E2-R	2.03	1.06	1.44	6.1	134	3.78	-0.9
HadGEM2-ES	0.61	0.49	1.54	7.5	98	2.93	-1.23
IPSL-CM5A-LR	0.79	0.57	1.14	8.1	100	3.1	-0.68
MPI-ESM-LR	1.21	0.62	1.42	8.5	78	4.09	-0.9

553 Table 2. Comparison of the distributions of GSAT anomaly (relative to 1986-2005) projected by
554 FaIR-TLM with the distributions of global-mean surface temperature assessed by AR5 (Collins
555 et al., 2013) in RCP 2.6, RCP 4.5, and RCP 8.5. Means are given without parentheses; likely
556 range (for AR5) and 17th-83th percentile range (for FaIR-TLM) are given in parentheses.
557

Period	AR5	FAIR-TLM
RCP 2.6 GSAT		
2046-2065	1.0 (0.4, 1.6)	0.86 (0.48, 1.21)
2081-2100	1.0 (0.3, 1.7)	0.83 (0.43, 1.21)
2181-2200	0.7 (0.1, 1.3)	0.69 (0.28, 1.06)
2281-2300	0.6 (0.0, 1.2)	0.57 (0.17, 0.92)
RCP 4.5 GSAT		
2046-2065	1.4 (0.9, 2.0)	1.29 (0.77, 1.77)
2081-2100	1.8 (1.1, 2.6)	1.67 (0.95, 2.32)
2181-2200	2.3 (1.4, 3.1)	2.10 (1.10, 3.02)
2281-2300	2.5 (1.5, 3.5)	2.39 (1.17, 3.49)
RCP 8.5 GSAT		
2046-2065	2.0 (1.4, 2.6)	1.93 (1.20, 2.61)
2081-2100	3.7 (2.6, 4.8)	3.49 (2.12, 4.75)
2181-2200	6.5 (3.3, 9.8)	6.76 (3.93, 9.46)
2281-2300	7.8 (3.0, 12.6)	8.04 (4.41, 11.45)
SSP3-7.0 GSAT		
2046-2065		1.60 (0.99, 2.17)
2081-2100		2.78 (1.69, 3.77)
2181-2200		5.16 (2.94, 7.24)
2281-2300		5.88 (3.10, 8.50)

Figure 1 Changes in DSL in response to changes in deep ocean temperature (first column) , global-mean surface air temperature (second column) in bivariate pattern scaling. The third column is the response of DSL changes to the warming in univariate pattern scaling. The first five rows display the maps of slopes obtained from a GCM over the period of 1981-2300. The sixth row shows the multi-model mean of slopes. The areas where sign agree in slopes among the five models are hatched. White areas are lands. Units for slopes are m K^{-1}.

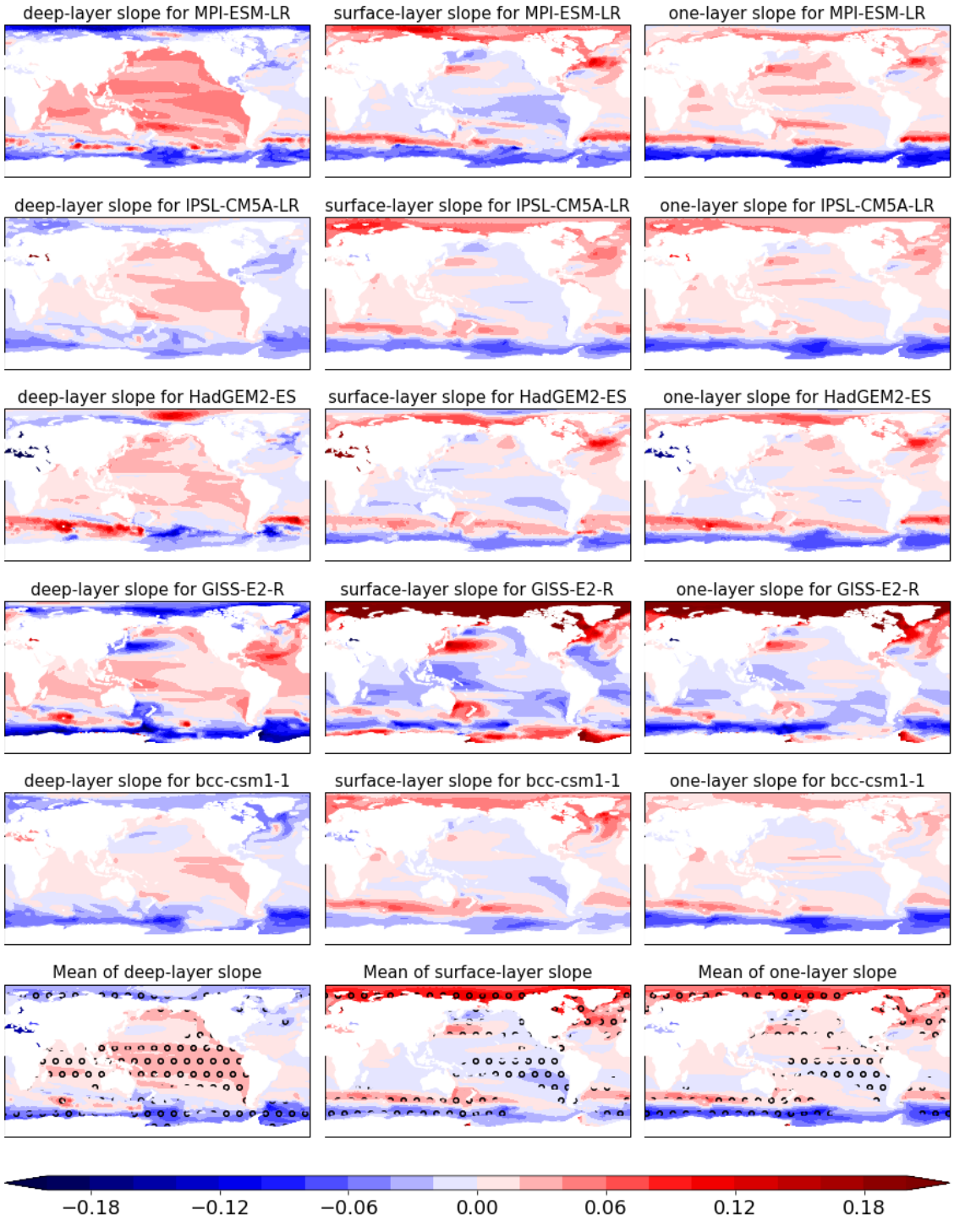

Figure 2 Differences between DSL simulated by GCMs (*zos*) and DSL($\widehat{zos}$) predicted by univariate pattern scaling (unvariate, first row) and two-layer pattern scaling (2-layer, second row) over the period 2271-2290 for the ensemble mean of 5 GCMs in three scenarios: RCP2.6, RCP4.5, RCP8.5 (Units: m). The third row shows the global mean of the $|zos - \widehat{zos}|$ in 1TS and 2TS, respectively. Black dots on maps denote the two grid cells used for the plot in Figure 3.

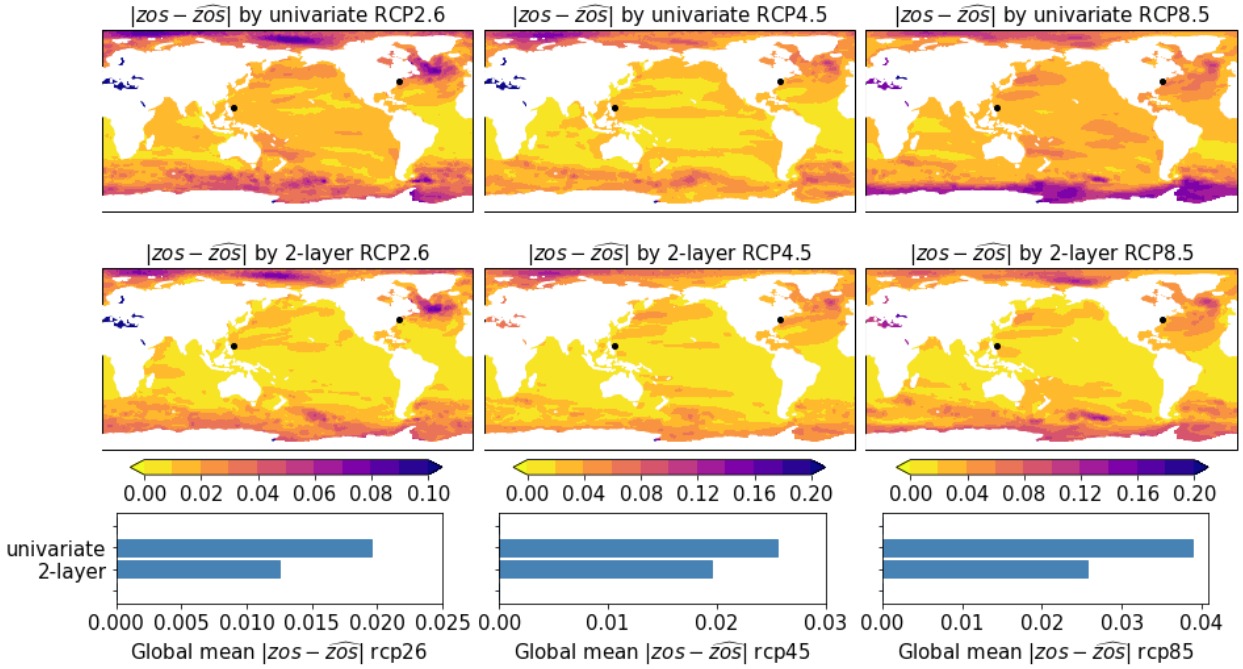

Figure 3. $\widehat{zos}$ predicted by univariate pattern scaling and 2-layer pattern scaling at the grid cell (a) over Western Pacific (14.5°N, 127°E) and (b) over the North Atlantic (40°N, 73°W) for the five models in the three scenarios. The *zos* simulated by corresponding GCMs is shown by scatters in which colors indicate years. Room mean square errors between the $\widehat{zos}$ and *zos* for each GCM are shown in parentheses of legend.

(a) Grid cell over Western Pacific

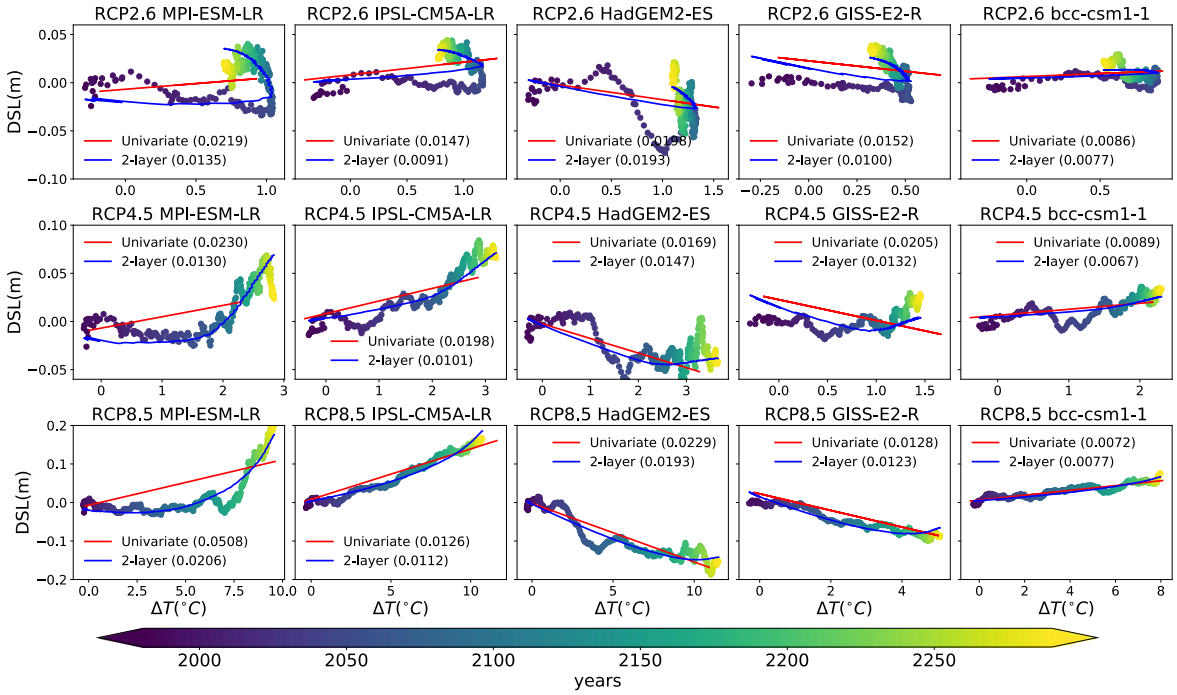

(b) Grid cell over North Atlantic

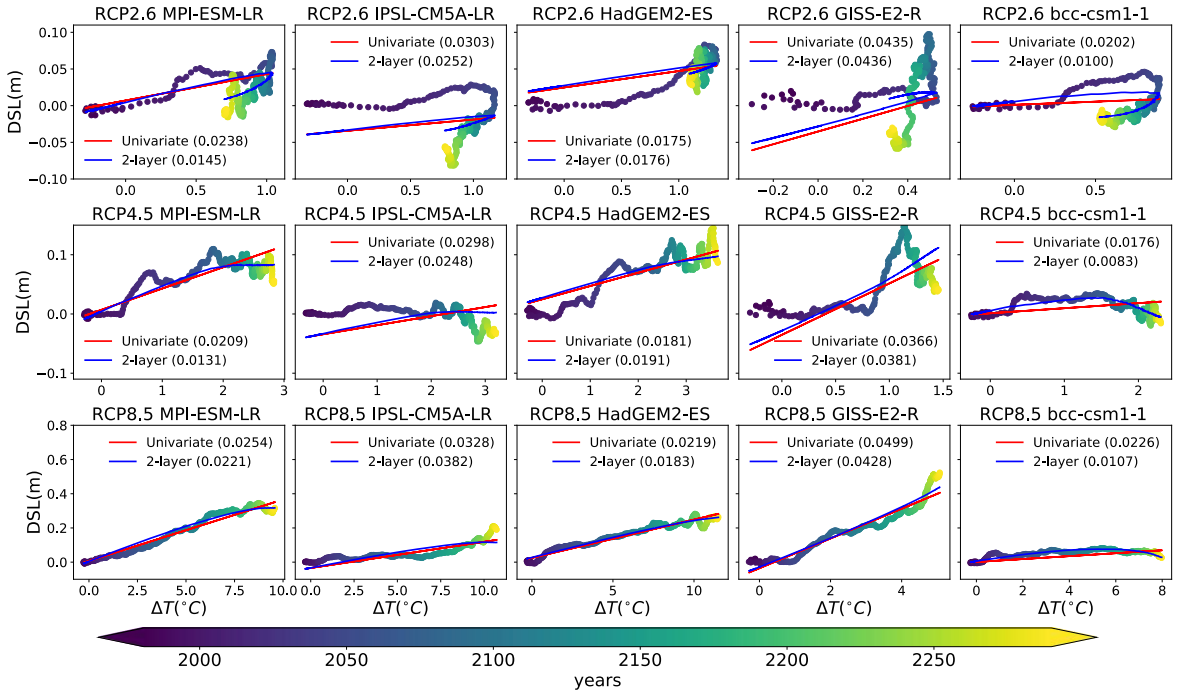

588 Figure 4. Ensemble projections of CO_2 concentrations (first row), GSAT (second row), deep-
589 ocean temperature (third row), and GMTSLR (fourth row) changes relative to the baseline period
590 1986-2005 under the four scenarios. Shadings represents the 66% range, dark blue lines the
591 median of 1000-member ensemble projections. The projection calibrated to the five GCMs in the
592 three RCP scenarios are shown on top of the shadings (orange lines).
593

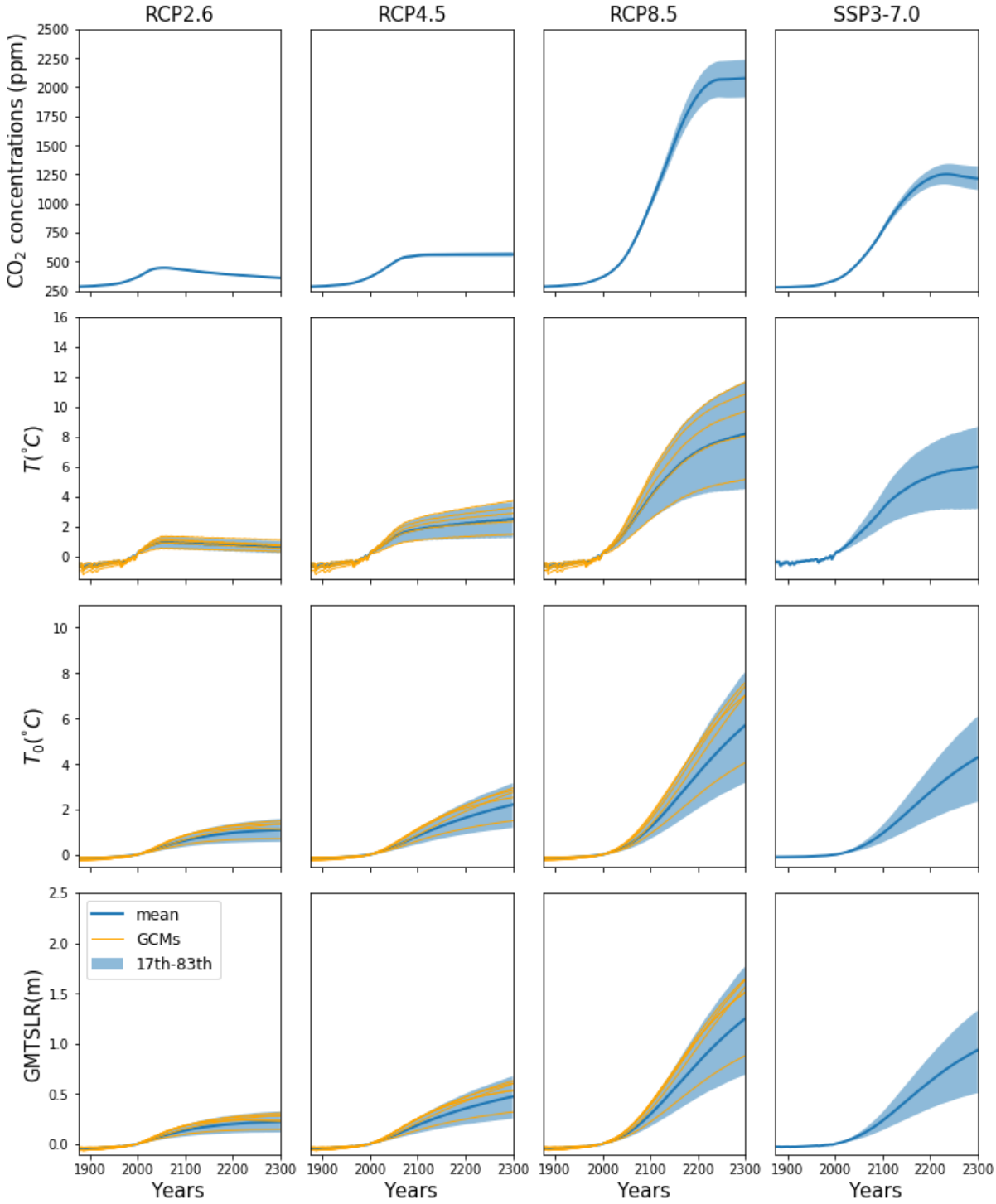

594
595

Figure 5. Projection of DSL changes at median estimation (first column) and range of 17th-83th percentile averaged over the period of 2081-2100 in four scenarios (a) relative to the baseline period 1986-2005. (b) is the same with (a) except for the period of 2271-2290. Units are m.

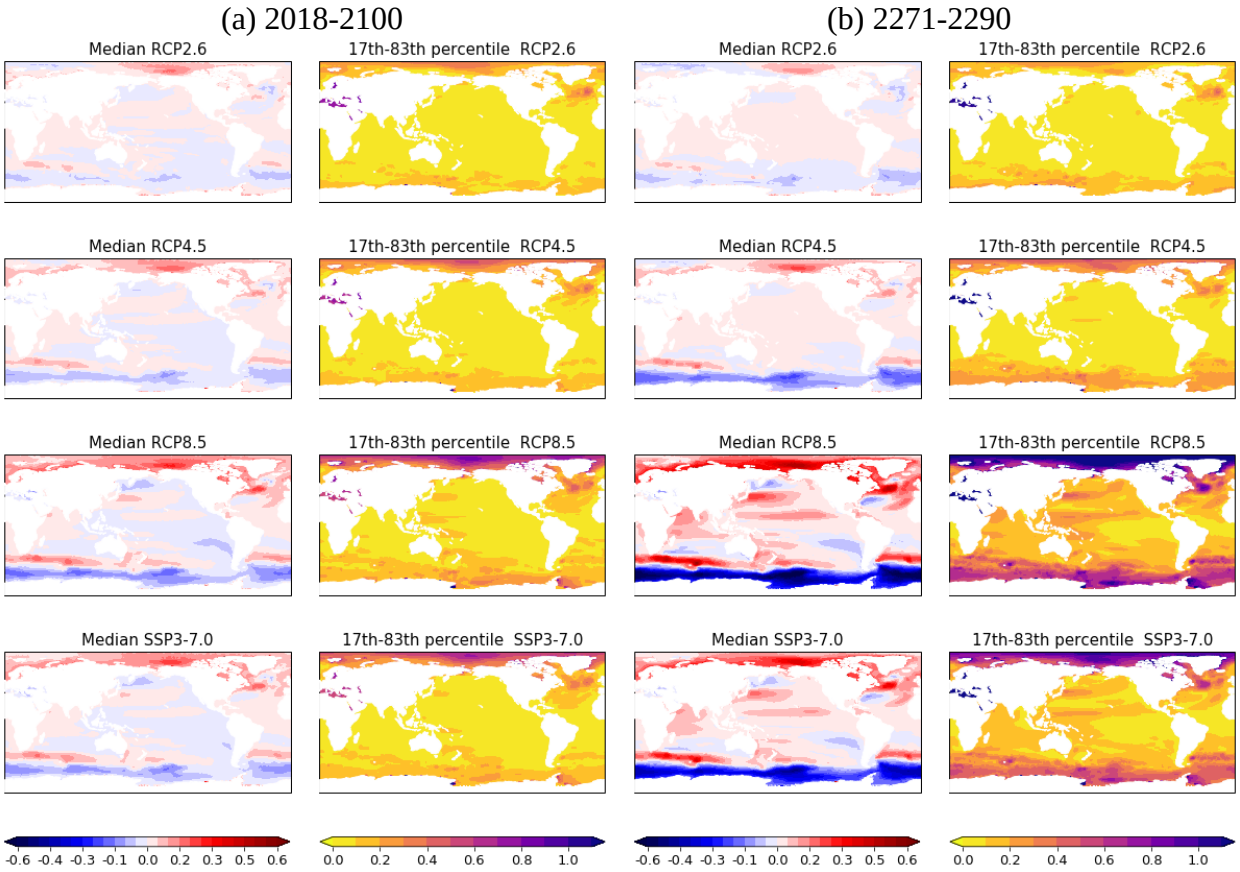

Figure 6. Ensemble projections of DSL changes relative to the baseline period 1986-2005 at the grid cells near Philippines over the western Pacific (upper panel) and near NYC over the North Atlantic (lower panel) for the four scenarios: RCP2.6, RCP4.5, RCP8.5 and SSP3-7.0. Light and dark shadings indicate the 90% and 66% range, respectively. Dark blue lines the median of 1000-member ensemble projections. The projection of DSL changes smoothed by 20-year running average in the five GCMs are shown on top of the shadings (colored lines).